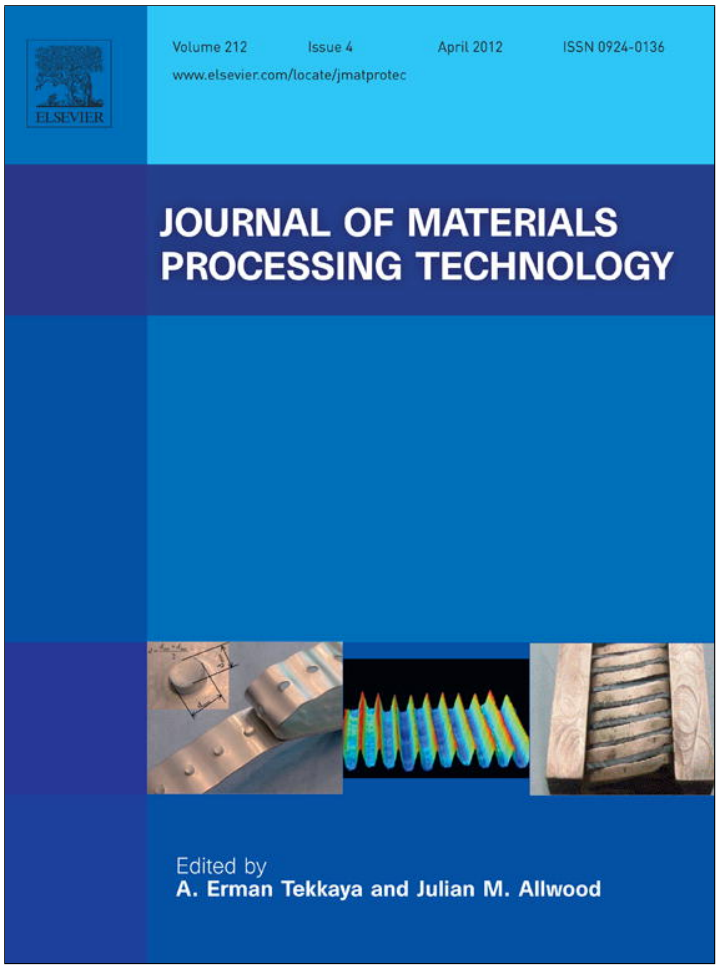

Journal of Materials Processing Technology 212 (2012) 856–867

Contents lists available at SciVerse ScienceDirect

Journal of Materials Processing Technology

journal homepage: www.elsevier.com/locate/jmatprotec

Laser beam welding of dissimilar stainless steels in a fillet joint configuration

M.M.A. Khan[a,*], L. Romoli[a], M. Fiaschi[b], G. Dini[a], F. Sarri[b]

[a] Department of Mechanical, Nuclear and Production Engineering, University of Pisa, Pisa, Italy
[b] Continental Automotive Italy S.p.A., Italy

ARTICLE INFO

Article history:
Received 8 February 2011
Received in revised form
17 November 2011
Accepted 20 November 2011
Available online 28 November 2011

Keywords:
Laser-welding
Dissimilar stainless steels
Constrained
Fillet joint

ABSTRACT

This paper investigates laser beam welding of dissimilar AISI 304L and AISI 430 stainless steels. Experimental studies were focused on effects of laser power, welding speed, defocus distance, beam incident angle, and line energy on weld bead geometry and shearing force. Metallurgical analysis was conducted on a selected weld only to show various microstructures typically formed at different zones and consequent change in microhardness. Laser power and welding speed were the most significant factors affecting weld geometry and shearing force. All the bead characteristics but radial penetration depth decreased with increased beam incident angle. The focused beam allowed selecting lower laser power and faster welding speed to obtain the same weld geometry. Weld shape factor increased rapidly due to keyhole formation for line energy input ranging from 15 kJ/m to 17 kJ/m. Fusion zone microstructures contained a variety of complex austenite–ferrite structures. Local microhardness of fusion zone was greater than that of both base metals.

1. Introduction

With the growing availability of new materials, industries, nowadays, utilize a variety of materials to make their products on a large scale with a view to improve performance and reduce cost. Among the various material combinations, the demands for using ferritic/austenitic (F/A) joints in power generation, chemical, petrochemical, nuclear and automotive industries are enormous (Sun, 1996). Thus, F/A joints are among one which has extensive industrial application in terms of production volume. This ultimately leads to an increased demand for techniques to weld these dissimilar materials and their use in large scale industrial production (Katayama, 2004). Of the available welding techniques, laser beam welding has received increasing attention due to rapid development in high-energy density beam technology in recent years (Kaiser and Schafer, 2005). Several researchers have reported the laser beam welding of dissimilar materials.

Li and Fontana (1998) investigated the COR_2R laser welding of AISI 304L and AISI 12L13 in butt joint configuration and found that the offset and the impingement angle of the laser beam are the two key parameters for controlling the melt ratio of the dissimilar materials. The strength of the laser welds was found to be higher than both the yield strength of AISI 304L and the rupture strength of AISI 12L13 under the test conditions adopted. Mai and Spowage (2004) conducted pulsed Nd:YAG laser autogenous welding of dissimilar metals for three different metal combinations and found no hot cracking in the welded joints. However, the porosity observed in the weld seam had a seemingly visible relationship with the welding speed. Liu et al. (2007) studied the parametric effects on seam morphology and mechanical properties of CW Nd:YAG laser welded dissimilar cast Ni-based super alloy K418 and alloy steel 42CrMo in butt configuration. X and T shape welded seam morphology were observed, and asymmetrical welded seam cross-section was obtained. The microhardness of the laser-welded seam was lower than the base metal. The strength of the joint was, however, equal to that of the base metal, and the fracture mechanism showed admirable ductility. Berretta et al. (2007) investigated the effects of laser position on the properties of two dissimilar AISI 304 and AISI 420 stainless steels. They found that joints obtained under all the welding conditions were uniform, and variations in beam position did not influence weld fillet geometry, which was typical of keyhole welding. Depending on the amount of shift of the laser beam position from the AISI 420 steel to AISI 304 steel, a gradual reduction in hardness along the cross-section of the weld zone was observed. Fracture occurred outside the weld zone in the tensile test. Besides, Mousavi and Sufizadeh (2009) examined the pulsed Nd:YAG laser welding of AISI 321 austenitic and AISI 630 (17-4PH) precipitation hardening stainless steels in a circular butt weld configuration focusing their studies on the effects of laser power, beam diameter and pulse duration on the depth and width of the welds. The results showed that both weld depth and weld width increased with voltage. The pulse duration had bilateral effects on the weld bead depth and width. Microhardness was found to be maximum and minimum respectively at AISI 630

* Corresponding author. Tel.: +39 0502218137.
E-mail address: muhshin.khan@ing.unipi.it (M.M.A. Khan).

0924-0136/$ – see front matter © 2011 Elsevier B.V. All rights reserved.
doi:10.1016/j.jmatprotec.2011.11.011

and AISI 321 sides. Pekkarinen and Kujanpää (2010) investigated to determine empirically the microstructural changes occurred in ferritic (AISI 430 & AISI 41003) and duplex (AISI 2205 and LDX 2101) stainless steels when heat input was controlled by welding parameter. Autogenous bead-on-plate welds were made without shielding gas using 5 kW fiber laser. Microstructures in both ferritic and duplex stainless steels were found to be dependent on composition and hence, welding parameters must be adjusted for each steel grade separately. With low-heat input, there was almost no martensite in AISI 430 stainless steels and grain size was high. Increasing heat input increased also the amount of martensite and decreased the grain size. The literatures support the fact that autogenous laser welding technique is suitable for producing weldable joints of dissimilar materials having considerable mechanical properties. Weld material, joint configuration, and welding parameters have significant effects on the weld seam characteristics, weld microstructure, the presence of defects and mechanical properties. Besides, it appears that laser welding of dissimilar ferritic AISI 430 and austenitic AISI 304L stainless steels in a circular and constrained fillet joint configuration has not been studied and reported yet. This is because this configuration complicates the joint design and requires accurate positioning of the focused beam at the corner. Otherwise, the focused beam can interfere with the vertical surface on its way to weld plane and reflect back to the adjacent horizontal surface making the welding process more complex.

Welding the dissimilar metals is still more challenging than that of similar metals due to the difference in the physical, mechanical, and metallurgical properties of the metals to be joined. Difference in thermal expansion coefficients of ferritic and austenitic steels may cause crack initiation at the interface, formation of hard zone close to weld interface, relatively soft regions adjacent to the hard zone, large hardness difference between hard and soft zones, and expected difference in microstructure leading to failure of the weld in service (Allabhakshi et al., 2002). Pan and Zhang (1996), on the other hand, report that micro-structural variations depend on the carbon content, the cooling rate, and the segregation of alloying elements. Proper selection of components, joint design, process, and process parameters are, therefore, mandatory to make the welds with desired properties during the laser welding of dissimilar ferritic and austenitic stainless steels.

1.1. Research objectives

Two tubular-shaped parts made of ferritic AISI 430 and austenitic AISI 304L stainless steels are assembled together ensuring a clearance between them and then welded circularly to produce the desired fillet joint. In these contexts, two possibilities emerge to solve the associated problems: adjustment of laser power, welding speed, and defocus distance or variation of the laser beam incident angle with respect to the vertical surface. In the first case, it is possible to control the energy input into the metals to be welded and hence heating and cooling rates of the weld pool, which can improve the metallurgical characteristics of the weld area. In the second case, control of melting ratio of two metals can compensate for the differences in absorption of the laser beam and the thermal conductivity. This paper, therefore, examines Nd:YAG laser welding of dissimilar ferritic and austenitic stainless steels in a constrained and circular fillet joint configuration. Experimental studies include the effects of above laser welding parameters on the weld bead characteristics such as weld width, penetration depth, radial penetration, resistance length, and shearing force. Effects of energy per unit length are also studied to show how energy input influences the weld bead characteristics, and to explain various phenomena related to laser welding. Finally, metallographic study is performed on a selected welded specimen only to demonstrate the microstructures that typically form at different zones and the consequent changes in local microhardness.

2. Materials and experimental procedures

2.1. Materials

Two tubular-shaped parts are made of ferritic AISI 430 (cold drawn, annealed and centerless ground) and austenitic AISI 304L (annealed, cold finished and centerless ground) stainless steels. These parts are welded circularly to make a fillet joint. This dissimilar joint is selected based on both technical and economical aspects, because they can provide satisfactory service performance and considerable savings. Moreover, in automotive industries, these materials are frequently used in welded form for making different types of fuel injectors. The chemical compositions of base metals available in as received condition and the weld seam characteristics are shown in Table 1 and Fig. 1 respectively. The inside diameter of the outer tube and the outside diameter of the inner tube are machined to Ø11.8 ± 0.025 mm and Ø11.758 ± 0.015 mm respectively to have a clearance between the parts when assembled. Inner (IT) and outer (OT) tubes are first assembled and then laser welded.

2.2. Laser experimental procedure

Specimens are welded circularly in a fillet joint configuration using a 1.5 kW continuous wave Nd:YAG laser (Rofin DY011). The optical system consisted of a 300 μm fiber and two lenses of 200 mm focal and collimate lengths are used to deliver the laser with a minimum focal spot diameter of 300 μm. A three-step procedure is followed to locate the focal point. First, an exceptionally sharp-nosed tool of 200 mm in height is attached to laser head mounted on Z motion stage. The laser head is then set to an intended beam incident angle. Finally, the positions of the X–Y–Z motion stages are adjusted in such a way that pointed tool tip touches the planned point of focus. Laser beam is focused on this located point through the laser head at the specified angle, and the necessary rotary motion is provided to the specimen through specimen holder mounted on an X–Y motion stage. Computer control panel is interfaced with the linear X–Y–Z as well as rotary motion systems to regulate the above said movements. Defocus distance is determined by changing the position of the focusing lens of the laser head in either a backward or a forward direction with a resolution of 0.025 mm.

The experiment is initially designed based on central composite rotatable design with full replication. During experimentation, laser power (P), welding speed (S), defocusing distance (D), and beam incident angle (A) are selected as process input variables for laser welding. Table 2 shows the experimental condition, laser

Table 1
Chemical compositions of base metals of the weld.

Base metals	Chemical compositions (%wt)								Thermal conductivity 298.2–1900 K (W/mK)
	C	Cr	Ni	Mn	P	S	Si	Fe	
AISI 304L	0.03	18.0–20.0	8.0–12.0	2.0	0.045	0.03	1.0	Rest	15–25.1
AISI 430	0.12	16.0–18.0	0.75	1.0	0.04	0.03	1.0	Rest	25–26.9

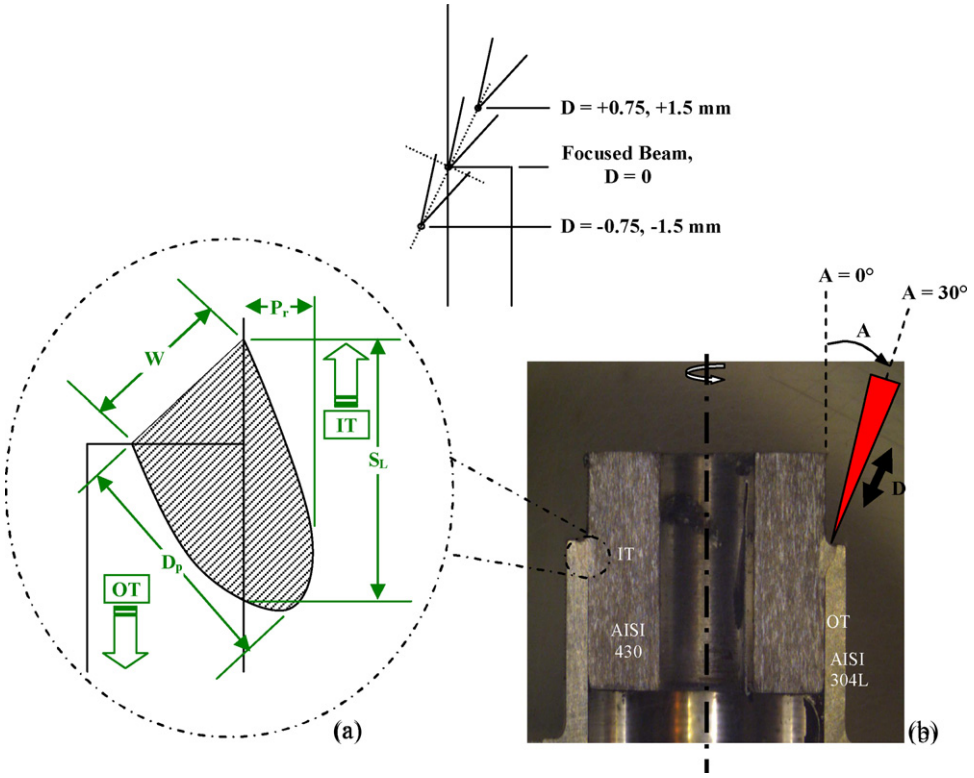

Fig. 1. Diagrams showing (a) bead characteristics of a welded fillet joint (W, weld width; S_L, weld resistance length; D_p, weld penetration depth; P_r, weld radial penetration) and (b) adopted laser-welding procedure.

welding input variables, and design levels used at a glance. Each of the input variables and its working range is selected based on industrially recommended laser-welding parameters used in automotive industries.

The energy delivered per unit length of weld line is referred to as line energy (LE), which is frequently used in various laser-processing techniques and termed as a key-parameter when continuous-wave laser is used. This term is calculated as the ratio of laser power over the welding speed as shown in Eq. (1):

$$\mathrm{LE} = 0.06\frac{P}{S}(\mathrm{kJ/m}) \quad (1)$$

where LE is line energy; P is laser power in watt (W) describing the thermal source; and S is welding speed in m/min determining the irradiation time. According to Eq. (1), the combinations of laser power of 600–1000 W and welding speed of 2.0–4.0 m/min resulted in nominal line energy input in the range of 12.0–24.0 kJ/m.

During the experiment, defocusing distance and laser beam incident angle are varied in the range of −1.5 to +1.5 mm and 10–30° respectively. Argon is used as shielding gas with a constant flow rate of 29 l/min to protect weld surface from oxidation, and to suppress the generation of plasma during welding. A standard washing procedure, which is practised in the automotive industries, is followed to clean, cool and dry the specimens.

In order to investigate the effects of line energy on the selected weld bead characteristics and shear force, line energy, defocus distance, and beam incident angle were varied in the range of 12.0–21.6 kJ/m, −0.75 to +0.75 mm and 10–30° respectively. Beam incident angle and defocus distance are kept constant at their central values to study the effects of defocus distance and beam

Table 2
Experimental conditions and response factors.

Process factors	Symbols	Actual values				
Laser power (W)	P	600	700	800	900	1000
Welding speed (m/min)	S	2.0	2.5	3.0	3.5	4.0
Angle of incidence (°)	A	10	15	20	25	30
Defocus distance (mm)	D	−1.5	−0.75	0	+0.75	+1.5

Constant factors		
Base material	Outer tube	AISI 304L
	Inner tube	AISI 430
Laser source	Continuous wave Nd:YAG laser	
Shielding gas	Type	Argon
	Flow rate	29 l/min

Response factors	
Weld bead characteristics	Weld width (W), weld penetration depth (D_p), weld radial penetration (P_r), and weld resistance length (S_L)
Weld mechanical properties	Weld shearing force (F_s)

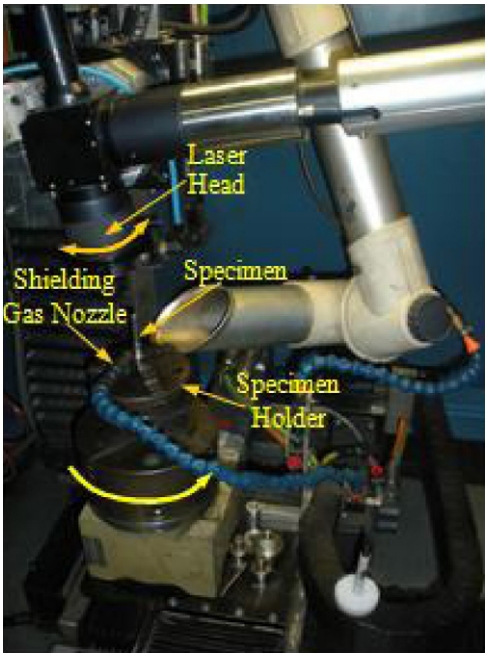

Fig. 2. Photographic view of Nd:YAG laser-welding system.

incident angle respectively. The experimental set-up for the laser-welding system is illustrated in Fig. 2.

2.3. Weld bead characterization

Welding tests are carried out in a random order to avoid any systematic error in the experiment. After welding, transverse sections are prepared by cutting the samples axially using SampleMet II (Beuhler, IL) model abrasive cutter. The sectioned samples are mounted, polished, and etched for mechanical characterization. Software, Leica IM500, incorporated with an optical microscope (Leica MZ125) is used to measure weld bead width, resistance length, radial penetration, and penetration depth. Push-out tests are also conducted to assess the shearing force of the weld. Each set of experiments is replicated three times to ensure statistical accuracy. The mean value of each measured response parameter is determined and recorded for further analysis. Table 3 shows the average measured responses for various laser-welding conditions.

The guidance on quality levels for imperfections given in ISO 13919-1:1996 is followed to assure the desired weld quality. At this point, each welded specimen is visually inspected before and after the cut using the optical microscope. Hermetic weld is ensured by performing leak test in vacuum for each of welded specimens. During leak test, nitrogen is inflated into the assembled part at a pulsed pressure in the range of 10–150 bar for the expected life cycles. This method also guarantees that the weld will not fail during its service life. In case of failure, the internal cracks generated during the welding process propagate up to the free surface and NR_2R leakage is detected by a loss of vacuum into the chamber.

As for the microstructural characterization, the selected sample is prepared and etched with kalling II solution (5 g CuCl2, 100 mL HCl, 100 mL ethanol). The microstructure is characterized by optical microscope (Reichert MF-2) and scanning electron microscopy (JEOL-JSM-5600 LV). Chemical composition of the weld material at various regions of the fusion zone is determined through energy dispersive spectrometer (EDS) analysis. The microhardness properties are assessed from inner to the outer tube by measuring the Vicker's microhardness along the line shown in Fig. 4.

3. Results

Various weld profile characteristics are measured with axially cut specimens using an optical microscope and are recorded for further analyses described in the succeeding sections.

Perturbation plots are used to illustrate the effects of individual process parameter such as laser power (P); welding speed (S); beam incident angle (A); and defocus distance (D) on the weld bead geometry and its mechanical properties. Contour plots are used to show the two-factor interaction effects of the selected process parameters on weld bead characteristics and shearing force.

The line energy is plotted against weld width, penetration depth, radial penetration, resistance length, and shearing force with a view to demonstrate the effects of energy input on weld profile characteristics as well as to explain different laser welding phenomena. Angular distortion associated with laser welding has also been analyzed.

3.1. Effect on weld bead characteristics

Fig. 3.1(a)–(d) shows the perturbation plots to compare the effects of all the process parameters at the center point in the design space. The results suggest that laser power has the most significant positive impact on the weld width, penetration depth, and resistance length, and a secondary effect on the weld radial penetration. The opposite phenomena are observed for the welding speed. These figures also illustrate that all the weld profile characteristics but the weld width decrease if the defocus distance changes from zero to positive and negative values. The weld width increases with the variation in defocus distance from its positive to negative values [Fig. 3.1(a)].

Except the initial beam incident angle ($A = 10^\circ$), as shown in Fig. 3.1(b)–(d), an increase in the angle of incidence leads to a decrease in both weld penetration depth and resistance length with an extension in radial penetration depth. It has a small or almost no effect on weld width as compared to other factors as can be noticed in Fig. 3.1(a).

The contour plots shown in Fig. 3.2(a)–(d) represent the facts that interactions of higher laser power and slower welding speed result in wider weld width; deeper weld penetration; larger radial penetration; and longer resistance length.

3.2. Effects on mechanical properties

3.2.1. Weld shearing force

The perturbation plot shown in Fig. 3.3(a) depicts that the weld shearing force increases with the laser power whereas decreases with the welding speed and the beam incident angle. It also decreases as the defocus distance varies from zero to positive and negative values. Linear, positive relationship between the weld shearing force and the resistance length can be observed in Fig. 3.3(b).

The contour plots, as illustrated in Figs. 3.2(d) and 3.4(a), show that higher laser power with slower welding speed results in longer weld resistance length with a consequent increase in shearing force. As shown in Fig. 3.4(a)–(c), it is possible to make a weld with similar shearing force for lower laser power and faster welding speed by adjusting the focused beam to the smallest possible incident angle.

3.2.2. Angular distortion

Laser welding of two coaxial inner and outer tubes in fillet joint configuration often results in misalignment with a consequent adverse effect on the performance of a fuel injector. The resulted misalignments that determine the angular distortion need to be checked and measured. A specialized run-out setup shown in

Table 3
Design matrix with actual factors and measured mean responses.

Standard order	Process factors				Response factors				
	P (W)	S (m/min)	A (deg)	D (mm)	W (mm)	S_L (mm)	P_r (mm)	D_p (mm)	F_s (kN)
1	700	2.5	15	−0.75	1.173	1.130	0.160	1.064	28.18
2	900	2.5	15	−0.75	1.573	1.337	0.240	1.368	30.04
3	700	3.5	15	−0.75	0.953	0.843	0.094	0.857	25.61
4	900	3.5	15	−0.75	1.272	1.223	0.173	1.137	29.02
5	700	2.5	25	−0.75	1.213	0.943	0.353	1.123	26.51
6	900	2.5	25	−0.75	1.250	1.150	0.466	1.390	28.36
7	700	3.5	25	−0.75	0.977	0.803	0.273	0.883	25.25
8	900	3.5	25	−0.75	1.000	0.977	0.387	1.189	26.81
9	700	2.5	15	0.75	1.263	1.097	0.167	1.203	27.89
10	900	2.5	15	0.75	1.543	1.457	0.293	1.457	31.12
11	700	3.5	15	0.75	1.020	0.880	0.130	0.990	25.94
12	900	3.5	15	0.75	1.375	1.330	0.200	1.240	29.98
13	700	2.5	25	0.75	1.050	0.940	0.320	0.980	26.48
14	900	2.5	25	0.75	1.100	1.040	0.430	1.320	27.38
15	700	3.5	25	0.75	0.499	0.790	0.200	0.810	25.13
16	900	3.5	25	0.75	0.950	0.952	0.316	1.093	26.59
17	600	3.0	20	0.00	1.040	0.830	0.140	0.890	25.49
18	1000	3.0	20	0.00	1.490	1.370	0.380	1.590	30.34
19	800	2.0	20	0.00	1.700	1.360	0.350	1.470	30.25
20	800	4.0	20	0.00	1.110	1.040	0.200	1.030	27.38
21	800	3.0	10	0.00	1.290	1.030	0.140	1.120	27.29
22	800	3.0	30	0.00	0.624	0.800	0.475	0.989	25.22
23	800	3.0	20	−1.50	0.637	1.260	0.150	0.968	29.35
24	800	3.0	20	1.50	1.050	1.021	0.130	0.987	27.21
25	800	3.0	20	0.00	1.340	1.220	0.240	1.270	28.99
26	800	3.0	20	0.00	1.390	1.080	0.340	1.250	27.74
27	800	3.0	20	0.00	1.270	1.000	0.270	1.200	27.02
28	800	3.0	20	0.00	1.370	1.130	0.290	1.260	28.18
29	800	3.0	20	0.00	1.270	1.150	0.300	1.240	28.36
30	800	3.0	20	0.00	1.390	1.240	0.220	1.260	29.17

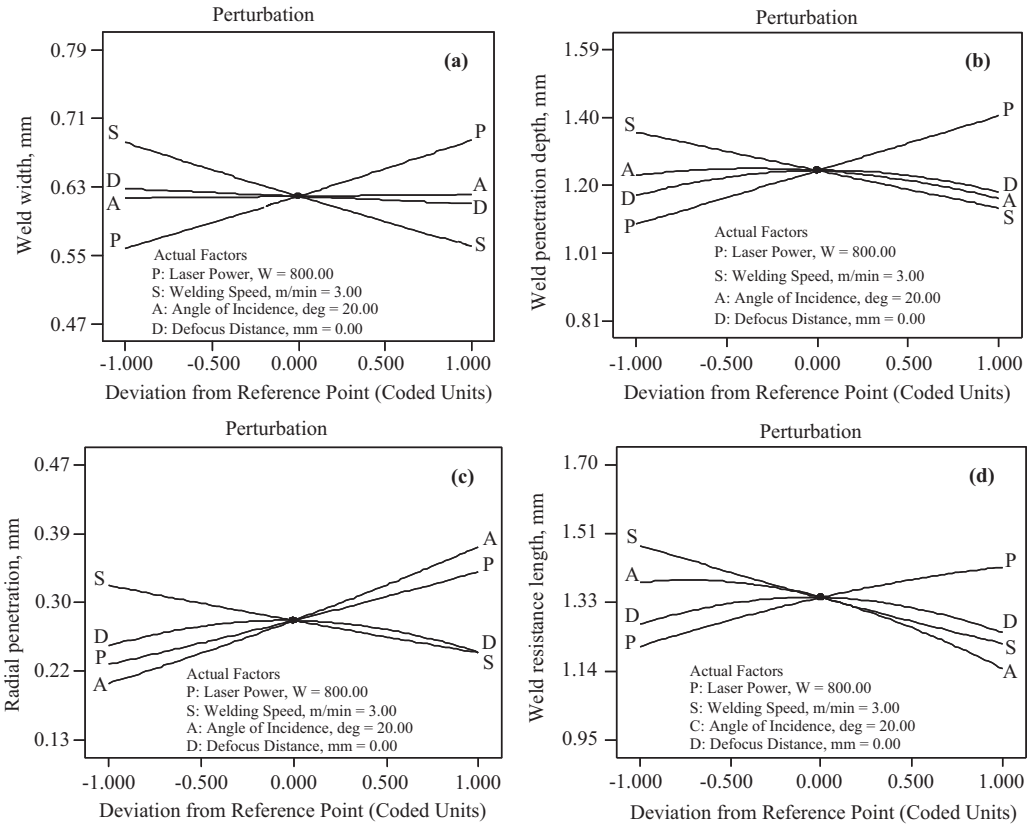

Fig. 3.1. Perturbation plot showing effect of all factors on (a) weld width, (b) weld penetration depth, (c) weld radial penetration, and (d) weld resistance length.

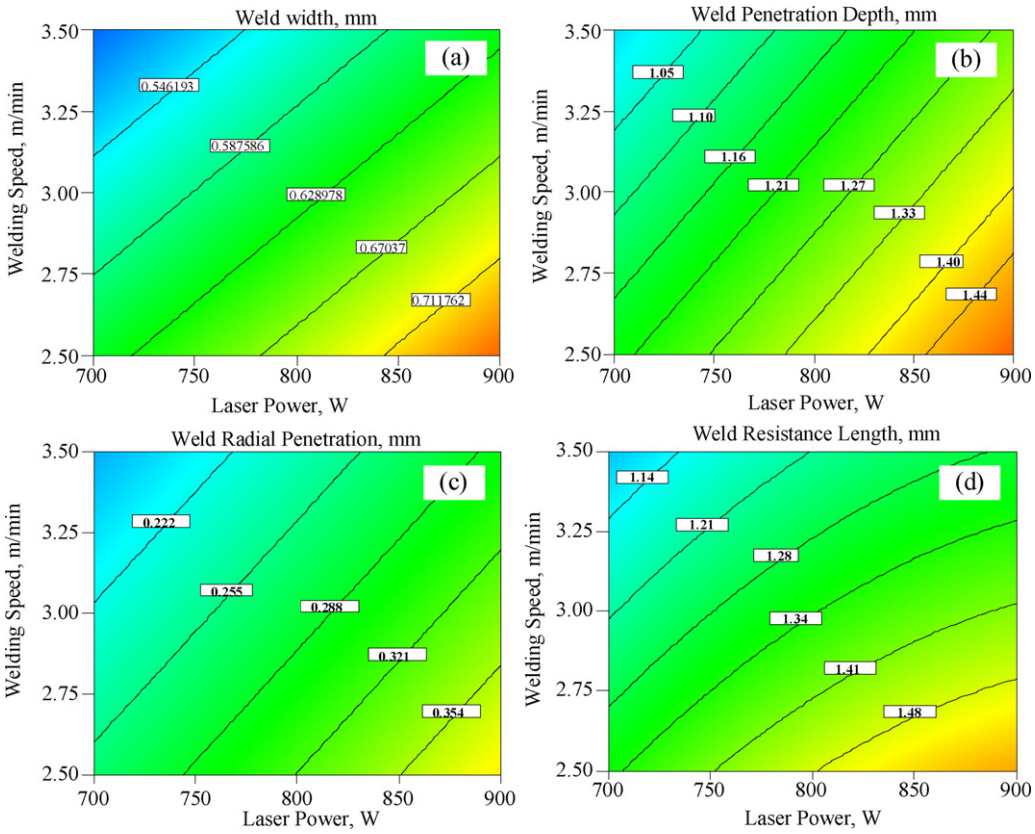

Fig. 3.2. Contour graphs to show the interaction effects of P and S on weld (a) width, (b) penetration depth, (c) radial penetration, and (d) resistance length at $A = 20^{\circ}$ and $D = 0.0$ mm.

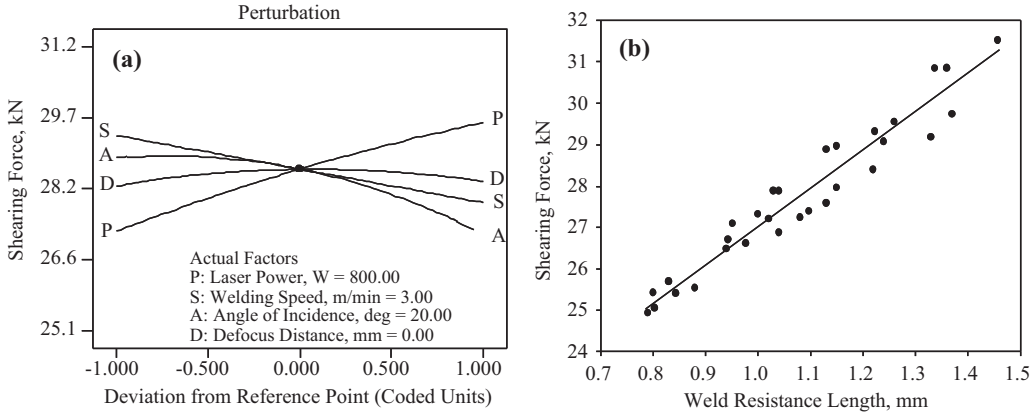

Fig. 3.3. (a) Perturbation plot showing effect of all factors on weld shearing force. (b) Relationship between weld shearing force and resistance length.

Fig. 3.5 is used for this purpose. Each welded specimen is mounted on the workpiece holder and rotated with the manual rotary motion mechanism. The total misalignment caused by the laser welding is measured by placing a displacement sensor at the top of the specimen. The values thus obtained for all the welded samples are observed to be random in the range of 25–250 μm. It is found that the angular distortion calculated is in the range of 0.06–0.35° only, which is much lesser than the allowable limit.

4. Discussion

4.1. Weld bead characteristics

Fig. 3.1(a)–(d) verifies that all the characteristic lengths featuring the weld geometry become larger as laser power increases or welding speed decreases. This is because higher laser power and slower welding speed result in higher energy deposition on the weld area, and longer irradiation time for the deposited energy to diffuse into material.

Reduction in weld penetration depth, radial penetration, and resistance length with respect to beam incident angle are also evident from Fig. 4.1(a)–(c). These phenomena are due to the following reasons: with an increase in beam incident angle, the direction of the laser beam focus changes from outer to the inner tube and the fraction of inner tube material become larger with a consequent rise in thermal conductivity of the weld molten mass. As a result, shallower weld penetration depth and shorter weld resistance length are achieved as explained by Wang et al. (1996).

At an incident angle, $A = 10^{\circ}$, the incident laser beam remains extremely close to sidewall. A fraction of beam energy gets lost

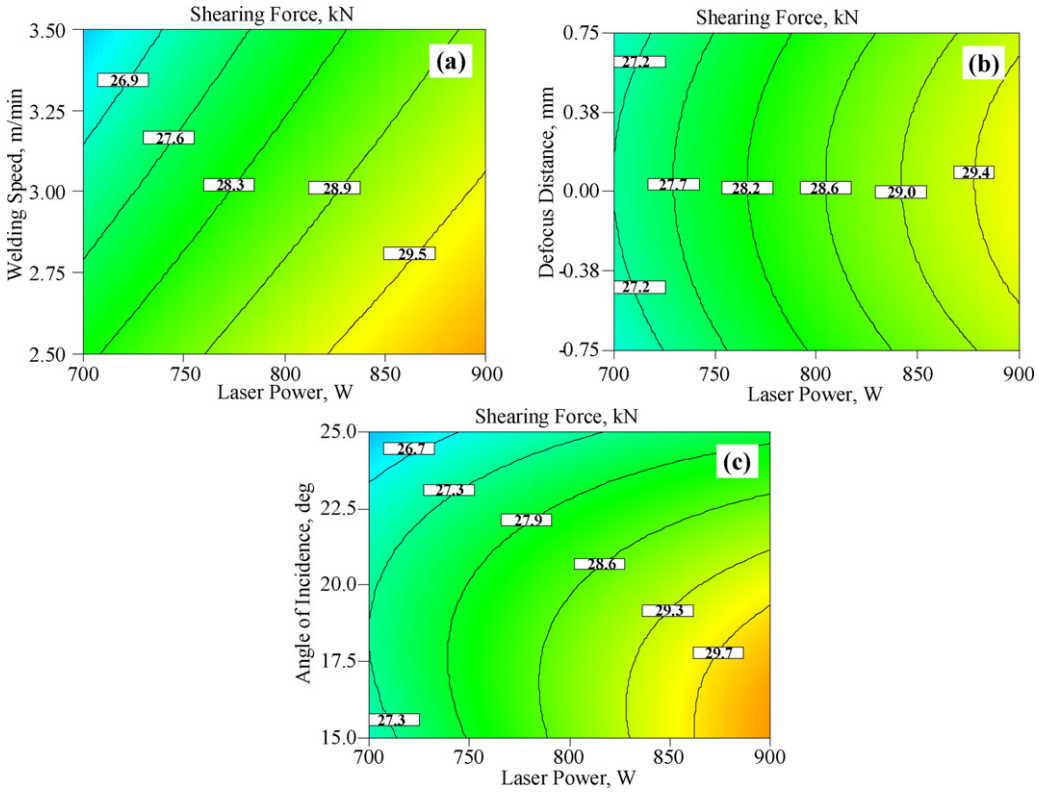

Fig. 3.4. Contour graphs to show the interaction effects of (a) *P* and *S*, (b) *D* and *P*, and (c) *A* and *P* on weld shearing force.

due to its interference with the vertical surface on its way to the weld plane and reflects back to the adjacent horizontal surfaces. These phenomena eventually widen the weld width and reduce the penetration depth and the resistance length. Since the axis of the weld moves away from the contact surface with a larger beam incident angle, weld radial penetration becomes longer.

The laser beam transfer characteristics reveal that the laser beam has the smallest spot diameter in the focal plane, which causes the highest energy density input into material. As a result, the deepest weld penetration, the longest radial penetration and the resistance length are achieved when the focused ($D = 0$) beam is used as shown in Figs. 3.1(b)–(d) and 4.2. When the laser beam is focused above weld plane, it diverges gradually while entering into the material. This results in lower energy input to the weld with a consequent decrease in the weld characteristics length. The effects are found to be somewhat higher when laser is focused below the weld plane. This is because the laser beam, in this case, converges gradually towards focal point and imparts higher amount of energy to the material. This facilitates diffusion of energy into greater depth favoring stronger melting and vaporization.

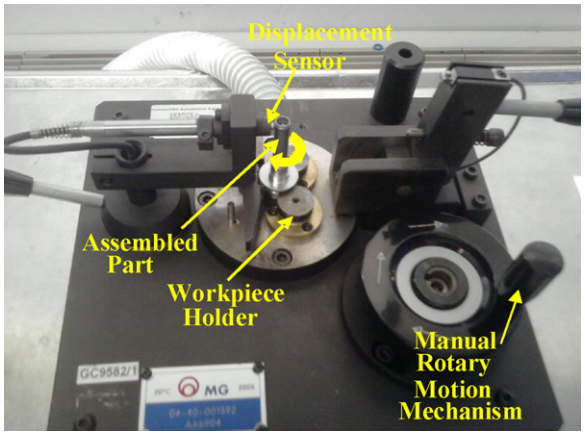

Fig. 3.5. Photographic view of the angular distortion test setup.

The positive relationship with weld width shown in Fig. 3.1(a) is due to the facts that negative defocused beam imposes higher energy to the weld material than positive defocused one, and the laser spot size increases sharply when its negative focal point distance exceeds the Rayleigh length as described by Cui et al. (2008).

Figs. 4.1 and 4.2 indicate that the weld penetration depth and radial penetration have linear, positive relationships with the line energy input. The weld resistance length, on the other hand, varies nonlinearly with it. These facts can be attributed to the existing linear and nonlinear interaction effects of laser power and welding speed as illustrated in Fig. 3.2(b)–(d). Khan et al. (2010) also disclose this linear dependence of weld penetration depth on energy input for welding martensitic stainless steels in an overlap joint design. The change in weld resistance length is more pronounced for the beam incident angle than the defocus distance. These variations are due to the establishment of different modes of laser welding with different ranges of line energy input.

The figures above (Figs. 4.1 and 4.2) clearly show that lower line energy input is needed to achieve the same weld penetration depth and resistance length when the laser beam is focused on the weld plane. An increase in beam incident angle intensifies the impact of energy input on weld radial penetration. Besides, any added energy input with a smaller beam incident angle results in deeper penetration depth and longer resistance length of the weld.

Fig. 4.3(a)–(b) shows the effects of line energy on the weld zone width. Since higher energy input leads to larger volume of melted materials, the weld width tends to increase with line energy input at the welded zone. Small change in weld width for different defocus distance and angle of incidence confirms the fact that these factors have an insignificant impact on it.

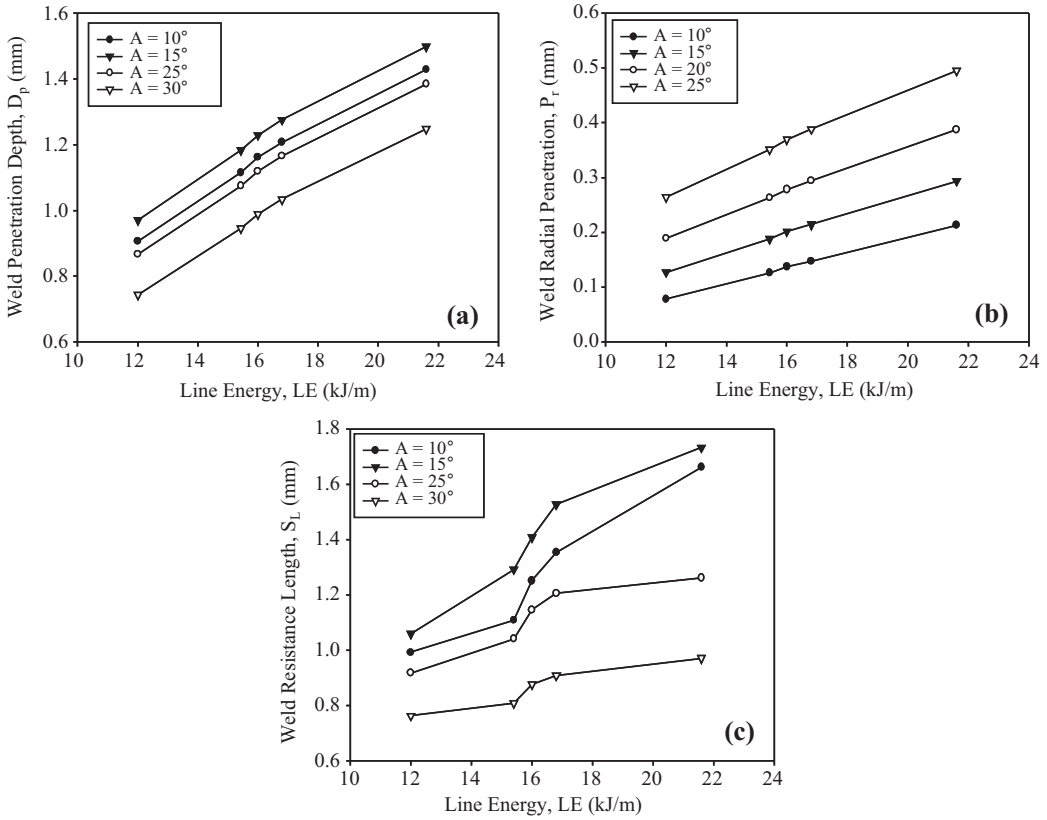

Fig. 4.1. Effect of line energy on weld (a) penetration depth, (b) radial penetration, (c) resistance length for different incident angles (A) at defocus distance, D = 0.0 mm.

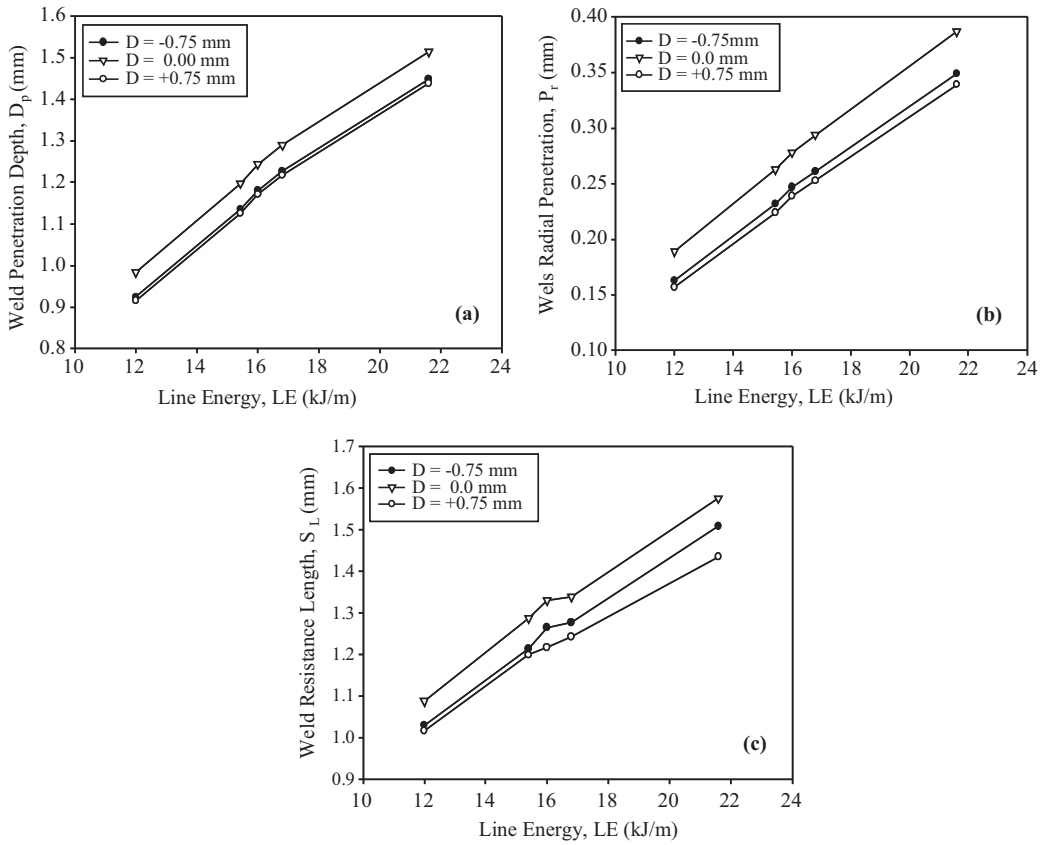

Fig. 4.2. Effect of line energy on weld (a) penetration depth, (b) radial penetration, (c) resistance length for different defocus distance (D) at incident angle, A = 20°.

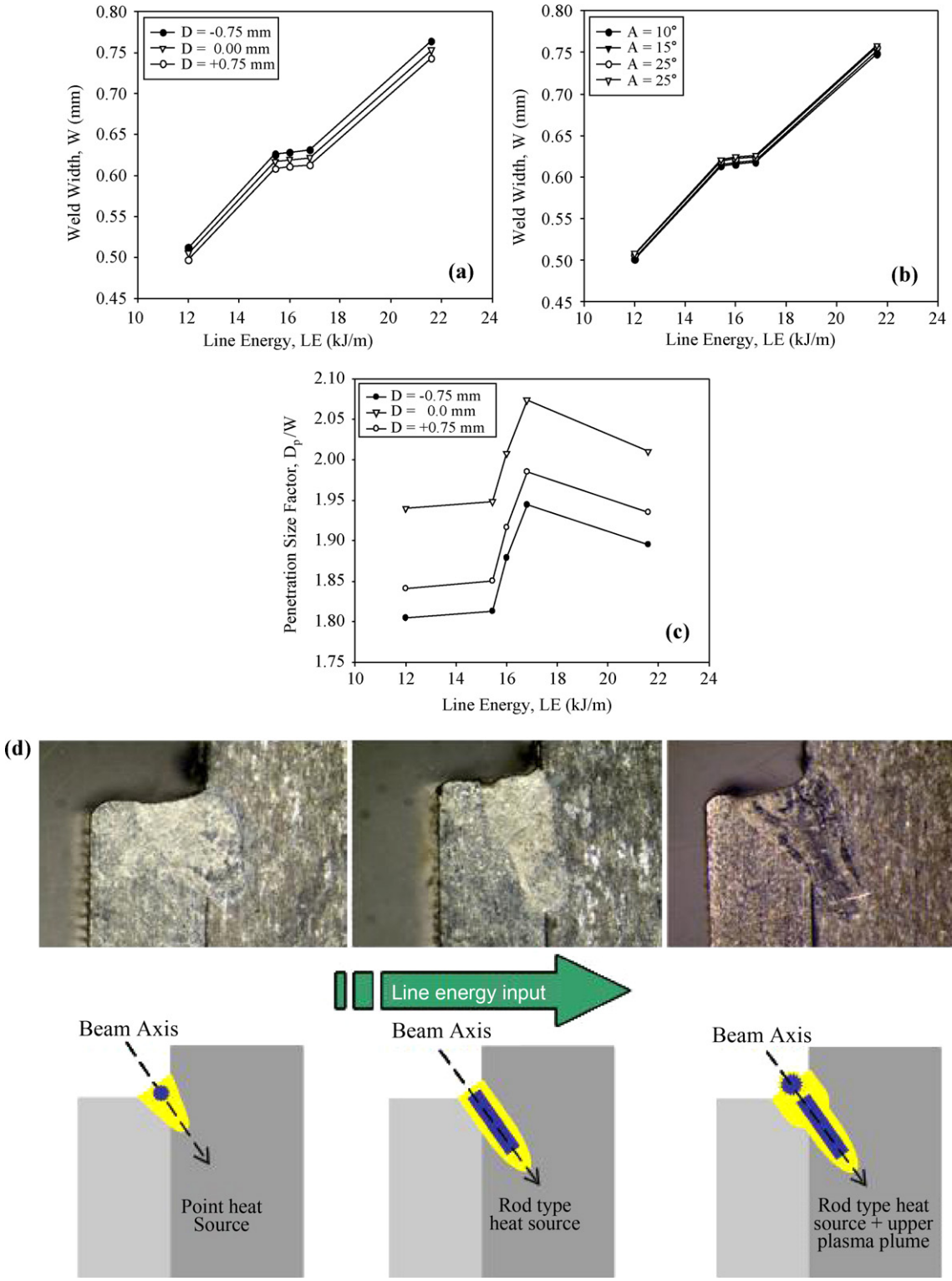

Fig. 4.3. Effect of line energy on weld width for different (a) defocus distance (D) at $A = 20^{\circ}$ and (b) angle of incidence (A) at $D = 0.0$ mm. (c) Effect of line energy on weld shape factor for different defocus distance at $A = 20^{\circ}$. (d) Pictorial and schematic views showing the change in shape factor with LE (i) conduction limited (12 to <15 kJ/m, (ii) keyhole formation (15–17 kJ/m), and (iii) keyhole with upper plasma plume (>17kJ/m).

For the line energy in the range of 12–15 kJ/m, as illustrated in Fig. 4.3(a)–(c), there is a rapid growth in weld width (W) with energy input, whereas change in shape factor (DR_pR/W) is negligible. Slight positive variations in weld shape factor prove that the laser welding is mainly conduction limited. Since the melt pool geometry depends on energy intensity, uniform conduction occurring in all directions usually results in semi-circular weld profile. However, the heat conduction along the beam axis becomes dominant with the increase in energy input and weld shape changes from semi-circular to parabolic.

There is almost no change in weld width when the line energy is in the range of 15–17 kJ/m. Nonetheless, a sharp rise (starting from

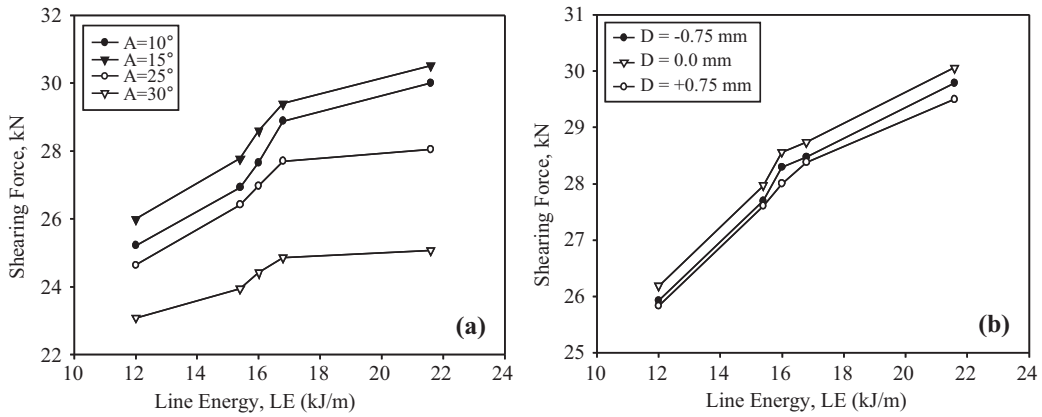

Fig. 4.4. Effect of line energy on weld shearing force for different (a) angle of incidence (A) at $D = 0.0$ mm and (b) defocus distance (D) at $A = 20^\circ$.

15 kJ/m) in D_p/W demonstrates the fact that the weld penetration depth increases at a faster rate than the weld width in this range and establishes a keyhole formation regime. As a result, the weld bead becomes almost cylindrical. Weld shape factor decreases with further increase in line energy. This is due to the creation of upper keyhole plasma plume that acts as a point heat source above weld plane. This generated plasma plume acts in the keyhole and forms a 'chalice' shaped weld bead profile when energy input is more than 17 kJ/m. Variation in weld shape factor for different laser welding modes is also illustrated pictorially as well as schematically in Fig. 4.3(d).

4.2. Weld shearing force

As shown in Fig. 4.4(a) and (b), a sharp rise in weld shearing force is also observed for the line energy input in the range of 15–17 kJ/m. This phenomenon can be described as a function of weld resistance length. It is worthmentioning that this resistance length increases rapidly within this range due to the establishment of a keyhole regime, and is linearly related to the resisting force to shear along the weld interface as can be seen in Figs. 4.2(c) and 3.3(b) respectively. Though their relationship shows a linear trend, dispersion of data from empirical straight line in Fig. 3.3(b) points out that failure due to shear might depend on microstructure formation and its alignment along the resisting section, which needs further investigation.

4.3. Weld microstructure

As shown in Fig. 4.5, metallurgical analyses are carried out to examine the microstructures forming at various locations of the fusion zone and the heat affected zones in the weld. The specimen is welded with a focused beam for the line energy input and the beam incident angle of 15.4 kJ/m and 25° respectively. This sample is selected as it ensures the minimum design criteria for the weld geometry and mechanical properties.

Fig. 4.6(a) shows that the fusion zone microstructure consists of mostly primary ferrite dendrites with an interdendritic layer of austenite. This austenite forms through a peritectic–eutectic reaction and exists at the ferrite solidification boundaries at the end of solidification. Some lathy ferrite morphology is also observed in this zone. This is due to restricted diffusion during ferrite–austenite transformation that results in a residual ferrite pattern.

Fig. 4.6(b) confirms that developed microstructures are a mixture of austenite and ferrite where Widmanstätten austenite nucleates from austenite along ferrite grain boundary. This is because solidification occurs as ferrite and no austenite forms at the end of solidification at this zone. As a result, this ferrite remains stable in the solid state at the elevated temperature. Austenite initially forms at the ferrite grain boundary when the ferrite structure cools below its solvus temperature. However, the transformation front breaks down and parallel needles of austenite form within the ferrite.

Fusion zone (FZ2) microstructures, as illustrated in Fig. 4.7, consist of austenite with ferrite along the solidification subgrain boundaries. This is because, during solidification, sufficient ferrite-promoting elements (particularly Cr) partition towards the solidification boundaries to promote the formation of ferrite as a terminal solidification product. The redistribution of principal alloying elements is reported in Table 4. The ferrite that forms along the boundary is relatively stable and resists transformation to austenite during weld cooling since it is already enriched in ferrite promoting elements. This solidification mode is termed as Type AF (austenite–ferrite) because it is associated with primary austenite solidification, where austenite is the first phase to form on solidification and ferrite forms at the end of the solidification process via an eutectic reaction.

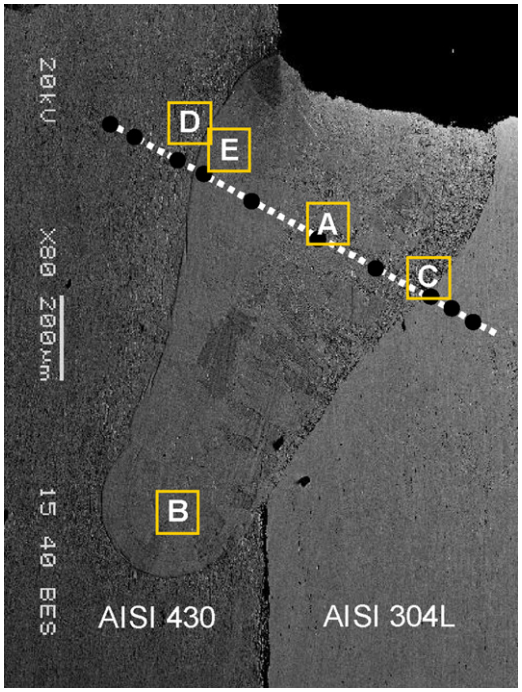

Fig. 4.5. Typical micrograph of laser welding of AISI 430 and AISI 304L stainless steels.

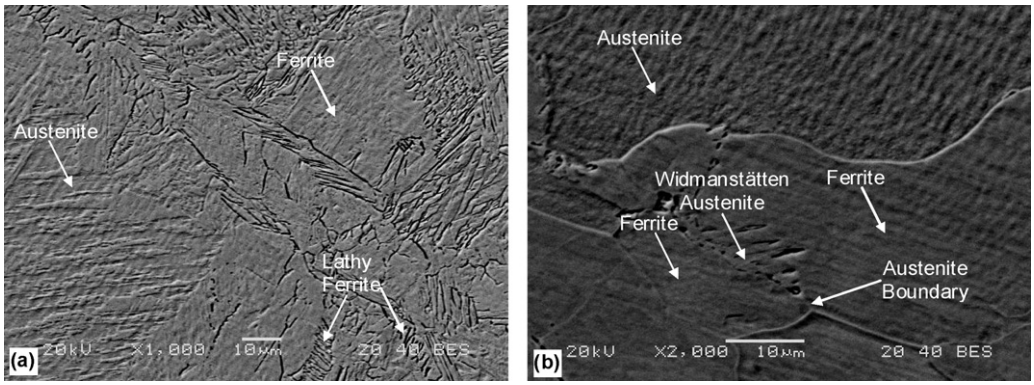

Fig. 4.6. Formation of microstructure in the fusion zone area indicated as (a) A and (b) B in Fig. 4.5.

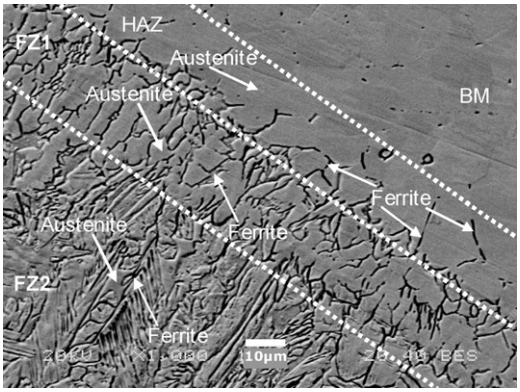

Fig. 4.7. Microstructures of as-supplied base metal, HAZ and fusion zone indicated as C in Fig. 4.5.

Microstructures, however, show distinct solidification structures (cells and dendrites) near the HAZ (FZ1) as these are fully austenitic at the end of solidification and remains austenite upon cooling to room temperature. This characteristic of solidification is due to the formation of primary austenite, the segregation of alloying and impurity elements that occur during solidification, and the relatively low diffusivity of these elements in the elevated temperature, which preserves the segregation profile that develops during solidification. Some ferrite also forms along the austenite grain boundary in the heat affected zone, which restrict the grain growth and minimize the susceptibility to HAZ liquation cracking.

Table 4
Redistribution of major alloying elements over the weld fusion zone.

Measured area indicated as	Weight percentage of major alloying elements (%wt) in fusion zone			
	Cr	Ni	Mn	Fe
A	18.16	6.37	1.57	72.8
B	18.55	3.05	1.02	77.2
C	17.76	7.16	1.95	75.6
E	19.22	4.89	1.16	76.9

Fig. 4.8(a) and (b) confirms that the microstructures of the base metal are the mixture of ferrite and carbides. The fusion zone microstructures, however, consist of a continuous layer of martensite along the ferrite grain boundaries and inter-granular $Cr_{23}C_6$ carbide precipitates. Primary solidification occurs solely as ferrite and remains stable over some temperature range at this zone. On cooling, some stable austenite forms and reprecipitation of $Cr_{23}C_6$ carbide occurs inter-granularly at the elevated temperature. Since the laser-welding is a self-quenching process, the austenite distributed normally along the ferrite grain boundaries transforms into martensite as the fusion zone cools rapidly to room temperature.

As shown in Fig. 4.8(a), two-phase ferrite and martensite is present in the heat affected zone. Intra-granular carbide formation is also evident. On cooling, precipitates normally form either inter- or intra-granularly with site based on cooling rate. Intra-granular precipitation typically occurs at high cooling rates while the creation of inter-granular precipitates is due to slow cooling rates.

4.4. Microhardness profile

Fig. 4.9 shows the microhardness profiles of the joint along the line shown in Fig. 4.5. The specimens selected for studying the change in local microhardness are made for two different beam

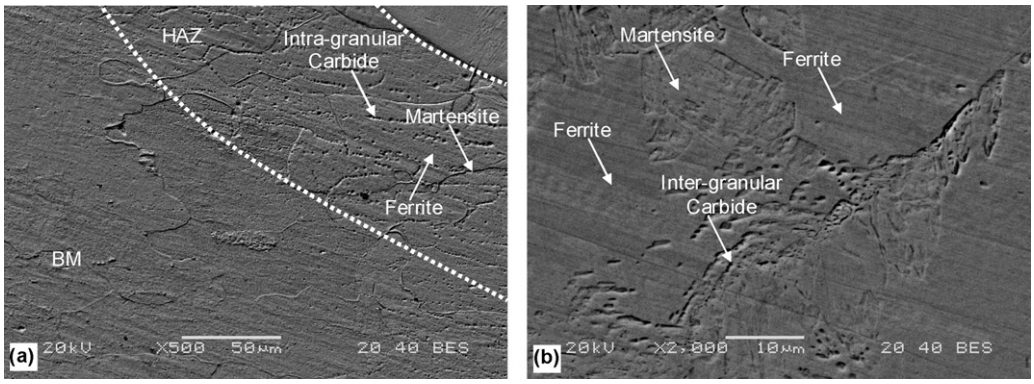

Fig. 4.8. Microstructure of (a) as-supplied base metal and HAZ indicated as D and (b) fusion zone indicated as E in Fig. 4.5.

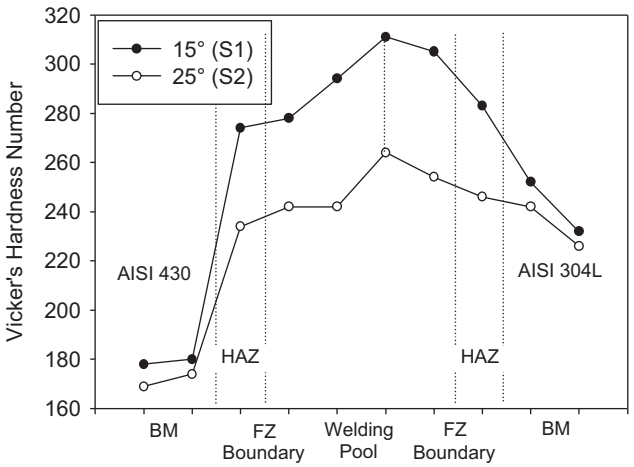

Fig. 4.9. Variation in local microhardness profile for different laser beam incident angles at LE = 15.4 kJ/m and $D = 0$.

incident angles. The line energy input and the defocus distance are kept constant during the experiment. The local microhardness of the fusion zone is greater than that of both base metals made of AISI 304L and AISI 430, which might have resulted from the effect of rapid solidification. As shown in Table 4, the microhardness gradient correlates with the gradient of the redistribution of elements Cr, Fe, and Ni. This is a remarkable phenomenon of dissimilar fusion joints.

The local microhardness measured at both sides of HAZ is lower than that of the fusion zone and higher than that of the respective base metals. This is due to the rapid solidification as mentioned earlier. Results of this study also demonstrate that local microhardness in the specimen S1 is higher than in the specimen S2. This can be attributed to the intermixture of increased percentage of austenitic stainless steel in the weld volume with the smaller beam incident angle.

5. Conclusion

Continuous wave Nd:YAG laser welding has been carried out on the ferritic/austenitic stainless steels. Parametric effects on the weld bead geometry and mechanical properties are investigated. The results can be summarized as follows:

- All the weld characteristics lengths and shearing force increases as laser power increase or welding speed decreases.
- Laser power has the most significant positive effect on all the characteristics lengths except the weld radial penetration. An increase in laser power only intensifies the effect of beam incident angle on radial penetration.
- The focused beam with lower laser power and faster welding speed produces a weld with the same weld geometry and shearing force.
- Beam incident angle is also found as a key factor that determines the weld bead geometry. The weld radial penetration increases significantly with beam incident angle whereas weld penetration depth, resistance length and hence shearing force decrease.
- A rapid increase in weld shape factor and shearing force with the line energy input in the range of 15–17 kJ/m depicts the establishment of a keyhole regime.
- Various, complex austenite–ferrite microstructures are identified in the fusion zone because of solidification behaviour and subsequent solid-phase transformation, which are controlled by composition and cooling rates.
- Formation of some ferrite along the austenite grain boundary in the heat affected zone on austenite side is observed. At the same time, microstructures are composed of two-phase ferrite and martensite with intra-granular carbide on ferrite side.
- Variation in local microhardness observed across the weld depends on the fraction intermix of each base metal and the redistribution of austenite- and ferrite-promoting elements in the weld.

Acknowledgements

Authors would like to acknowledge Continental "Cleanliness and Material Lab" for its support while cutting and preparing the samples for analysis. The help extended by V. Colombini and C. Fierro during experimental investigation is also sincerely acknowledged. Sincere thanks are offered to Dr. M.S. Sureshkumar, Associate Professor, Saveetha University, India for his valuable suggestions while revising the discussion section.

References

Allabhakshi, S., Madhusudhan Reddy, G., Ramarao, V.V., Phani Babu, C., Ramachandran, C.S., 2002. Studies on weld overlaying of austenitic stainless steel (AISI 304) with ferritic stainless steel (AISI 430). In: Proceedings of the National Welding Conference, Indian Institute of Welding, Chennai, India (Paper 8).

Berretta, J.R., de Rossi, W., Neves, M.D.M., de Almeida, I.A., Junior, N.D.V., 2007. Pulsed Nd:YAG laser welding of AISI 304 to AISI 420 stainless steels. Optics and Lasers in Engineering 45, 960–966.

Cui, C., Hu, J., Gao, K., Pang, S., Yang, Y., Wang, H., Guo, Z., 2008. Effects of process parameters on weld metal keyhole characteristics with COR_2R laser butt welding. Lasers in Engineering 18, 319–327.

Kaiser, E., Schafer, P., 2005. Pulse sharpening optimizes the quality of seam and spot welds. In: Lasers in Manufacturing, Proceeding of the Third International WLT Conference on Lasers in Manufacturing, pp. 695–698.

Katayama, S., 2004. Laser welding of aluminium alloys and dissimilar metals. Weld International 18 (8), 618–625.

Khan, M.M.A., Romoli, L., Fiaschi, M., Dini, G., Sarri, F., 2010. Experimental investigation on laser beam welding of martensitic stainless steels in a constrained overlap joint configuration. Journal of Materials Processing Technology 210, 1340–1353.

Li, Z., Fontana, G., 1998. Autogenous laser welding of stainless steel to free-cutting steel for the manufacture of hydraulic valves. Journal of Materials Processing Technology 74, 174–182.

Liu, X.B., Yu, G., Pang, M., Fan, J.W., Wang, H.H., Zheng, C.Y., 2007. Dissimilar autogenous full penetration welding of superalloy K418 and 42CrMo steel by a high power CW Nd:YAG laser. Applied Surface Science 253, 7281–7289.

Mai, T.A., Spowage, A.C., 2004. Characterisation of dissimilar joints in laser welding of steel–kovar, copper–steel and copper–aluminium. Materials Science and Engineering A 374, 224–233.

Mousavi, S.A.A.A., Sufizadeh, A.R., 2009. Metallurgical investigations of pulsed Nd:YAG laser welding of AISI 321 and AISI 630 stainless steels. Materials and Design 30, 3150–3157.

Pan, C., Zhang, E., 1996. Morphologies of the transition region in dissimilar austenitic–ferritic welds. Materials Characterization 36 (1), 5–10.

Pekkarinen, J., Kujanpää, V., 2010. The effects of laser welding parameters on the microstructure of ferritic and duplex stainless steels welds. Physics Procedia 5, 517–523.

Sun, Z., 1996. Feasibility of producing ferritic/austenitic dissimilar metal joints by high energy density laser beam process. International Journal of Pressure Vessels and Piping 68, 153–160.

Wang, S.C., Wang, C., Tu, Y.K., Hwang, C.J., Chi, S., Wang, W.H., Cheng, W.H., 1996. Effect of Au coating on joint strength in laser welding for invar-invar packages. In: Electronic Components and Technology Conference, IEEE, pp. 942–945.